energies

MDPI

Article

Influence of Temperature and Bedding Planes on the Mode I Fracture Toughness and Fracture Energy of Oil Shale Under Real-Time High-Temperature Conditions

Shaoqiang Yang [1,2,*], Qinglun Zhang [1] and Dong Yang [3]

[1] College of Engineering for Safety and Emergency Management, Taiyuan University of Science and Technology, Taiyuan 030024, China; qinglun@stu.tyust.edu.cn
[2] Intelligent Monitoring and Control of Coal Mine Dust Key Laboratory of Shanxi Province, Taiyuan 030024, China
[3] Key Laboratory of In Situ Property-Improving Mining of Ministry of Education, Taiyuan University of Technology, Taiyuan 030024, China; yangdong@tyut.edu.cn
* Correspondence: yangshaoqiang@tyust.edu.cn

Abstract: The anisotropic fracture characteristics of oil shale are crucial in determining reservoir modification parameters and pyrolysis efficiency during in situ oil shale pyrolysis. Therefore, understanding the mechanisms through which temperature and bedding planes influence the fracture behavior of oil shale is vital for advancing the industrialization of in situ pyrolysis technology. In this study, scanning electron microscopy (SEM), CT scanning, and a real-time high-temperature rock fracture toughness testing system were utilized to investigate the spatiotemporal evolution of pores and fractures in oil shale across a temperature range of 20–600 °C, as well as the corresponding evolution of fracture behavior. The results revealed the following: (1) At ambient temperature, oil shale primarily contains inorganic pores and fractures, with sizes ranging from 50 to 140 nm. In the low-temperature range (20–200 °C), heating primarily causes the inward closure of inorganic pores and the expansion of inorganic fractures along bedding planes. In the medium-temperature range (200–400 °C), organic pores and fractures begin to form at around 300 °C, and after 400 °C, the number of organic fractures increases significantly, predominantly along bedding planes. In the high-temperature range (400–600 °C), the number, size, and connectivity of matrix pores and fractures increase markedly with rising temperature, and clay minerals exhibit adhesion, forming vesicle-like structures. (2) At room temperature, fracture toughness is highest in the Arrester direction ($K_{IC\text{-}Arr}$), followed by the Divider direction ($K_{IC\text{-}Div}$), and lowest in the Short-Transverse direction ($K_{IC\text{-}Shor}$). As the temperature increases from 20 °C to 600 °C, both $K_{IC\text{-}Arr}$ and $K_{IC\text{-}Div}$ initially decrease before increasing, reaching their minimum values at 400 °C and 500 °C, respectively, while $K_{IC\text{-}Shor}$ decreases continuously as the temperature increases. (3) The energy required for prefabricated cracks to propagate to failure in all three directions reaches a minimum at 100 °C. Beyond 100 °C, the absorbed energy for crack propagation along the Divider and Short-Transverse directions continues to increase, whereas for cracks propagating in the Arrester direction, the absorbed energy exhibits a 'W-shaped' pattern, with troughs at 100 °C and 400 °C. These findings provide essential data for reservoir modification during in situ oil shale pyrolysis.

Keywords: real-time high temperature; thermal crack; pore evolution; fracture characteristics; oil shale

Citation: Yang, S.; Zhang, Q.; Yang, D. Influence of Temperature and Bedding Planes on the Mode I Fracture Toughness and Fracture Energy of Oil Shale Under Real-Time High-Temperature Conditions. *Energies* **2024**, *17*, 5344. https://doi.org/10.3390/en17215344

Academic Editor: Reza Rezaee

Received: 6 October 2024
Revised: 24 October 2024
Accepted: 25 October 2024
Published: 27 October 2024

1. Introduction

Under natural conditions, oil shale is a fine-grained sedimentary rock that is rich in organic matter and characterized by a high ash content [1]. Oil shale typically exhibits a dense structure with low permeability. The kerogen contained within oil shale is insoluble in conventional organic solvents, making it unsuitable for exploitation as a source of oil

and gas through conventional methods. However, when subjected to high-temperature pyrolysis, the kerogen can release shale oil and mixed hydrocarbon gases [2]. With the increasing global demand for oil and gas resources and the decline of conventional petroleum reserves, oil shale holds significant potential to offset the future global energy shortfall due to its large reserves—four times greater than those of conventional petroleum—and widespread distribution [3–5].

Surface retorting and in situ pyrolysis are the two primary methods currently used for oil shale extraction. In situ pyrolysis is considered the only viable technology for the industrial-scale exploitation of oil shale due to its minimal environmental impact and significantly lower production costs, which are only 1/20th of those associated with surface retorting [6–8]. Given the poor thermal conductivity of oil shale, achieving rapid heating of the formation is crucial for reducing extraction costs. The convective heating in situ pyrolysis technology, known as MTI technology, developed by Taiyuan University of Technology, is distinguished by its rapid heating rates and high production capacity [3,9]. This technique first involves reservoir modification through hydraulic fracturing, followed by the use of high-temperature steam (exceeding 550 °C) as a heat carrier to achieve convective heating of the oil shale formation. In this process, the fractures created by hydraulic fracturing serve not only as the main channels for steam injection and product extraction but also as the primary sites for the pyrolysis of organic matter. However, the stress field changes within the formation due to heating can lead to the further propagation or closure of these fractures, thereby affecting fluid migration and determining the extent of the pyrolysis zone. Fracture toughness, an inherent material property, reflects the ability of a cracked material to resist further crack propagation and is a critical parameter for determining hydraulic fracturing conditions [10]. The mechanical anisotropy of oil shale, influenced by bedding planes and the presence of organic matter, affects the competitive propagation of pre-existing fractures and newly formed hydraulic fractures during the fracturing process [11–13]. After the initial pyrolysis in the first extraction area is completed, subsequent reservoir modifications in target pyrolysis zones will involve transitioning from a low-temperature to a high-temperature environment. Therefore, it is essential to study the fracture evolution of oil shale under high-temperature conditions to ensure the successful implementation of the in situ pyrolysis process.

As a sedimentary rock, oil shale exhibits significant mechanical anisotropy due to the preferred orientation of its mineral components, the presence of organic matter, and bedding fractures [14–16]. Current research on the fracture anisotropy of jointed rocks primarily focuses on factors such as bedding orientation, mineral composition, size effects, deformation rates, and tectonic stress conditions [17–21]. Shi et al. investigated the relationship between fracture toughness, elastic modulus, and wave velocity of Longmaxi shale with respect to bedding planes. They found that the maximum fracture toughness of Longmaxi shale is twice the minimum value, with fracture toughness positively correlated with the bedding angle, while the elastic modulus and wave velocity are negatively correlated with the bedding angle [17]. Xiong et al. discovered that shale fracture toughness is positively correlated with the content of clay minerals and negatively correlated with the content of brittle minerals, with high temperatures and fluids reducing shale fracture toughness [18]. Rey et al. examined the variation in fracture toughness of granite with sample size, finding a strong correlation where larger sample sizes yielded greater fracture toughness [19]. Shi et al. used the split Hopkinson pressure bar (SHPB) system to study the dynamic fracture toughness characteristics of black shale and found that fracture toughness increases with loading rate and rises with increasing loading angle at the same rate [20]. Shi et al. also investigated the relationship between shale fracture toughness and confining pressure in in situ deep conditions, revealing that both Mode I fracture toughness (K_{IC}) and fracture energy (GIC) increase significantly with confining pressure and exhibit distinct anisotropy under various confining pressures [21]. While substantial progress has been made in understanding the fracture toughness anisotropy of rocks at room temperature, fur-

ther research is needed to explore the effects of high temperatures on the fracture evolution of oil shale during in situ pyrolysis processes.

Temperature is a crucial factor affecting the mechanical properties of rocks and has long been a focus of research in various fields, including deep shale gas extraction, geothermal resource development, in situ thermal cracking of oil and gas resources, and nuclear waste storage [22–26]. Depending on the engineering context, existing studies have primarily concentrated on rocks such as granite, sandstone, shale, and limestone [22,27–29]. These studies have considered factors such as strain rate, chemical environment, and bedding orientation, all of which impact physical and mechanical properties like fracture toughness, acoustic emission characteristics, and wave velocity [10,27,30,31]. Suo et al. investigated the changes in fracture toughness of deep shale under different strain rates within a temperature range of room temperature to 190 °C. They found that peak load increases with loading rate, while fracture toughness decreases with rising temperature, and acoustic emission intensifies near the stress peak [30]. Chang's study revealed that after five thermal shocks at 150 °C, shale developed numerous tensile cracks, leading to a 25.9% reduction in fracture toughness [10]. Kang et al. examined the variations in Mode I and Mode II fracture toughness of granite subjected to thermal treatments ranging from 20 °C to 900 °C. They found that the greatest reduction in tensile strength occurred in the 20–300 °C and 300–600 °C temperature ranges for Mode I and Mode II fractures, respectively, while the 20–300 °C range showed the greatest reduction for mixed-mode fractures [31]. Significant progress has been made in understanding the fracture evolution of rocks after exposure to high temperatures; however, the internal thermal stress and cohesion of rocks under real-time high temperatures differ markedly from those observed after thermal exposure [32]. To address this, Funatsu used oil as a heating medium to study the variation in the fracture evolution of sandstone within a temperature range from room temperature to 200 °C, discovering that fracture toughness decreased continuously from room temperature to 75 °C but increased from 100 °C to 200 °C [33]. Closmann investigated the tensile and compressive strengths of oil shale under high temperatures ranging from 20 °C to 400 °C, finding that both strengths decreased with rising temperature, with the elastic modulus at 400 °C being only 51% of its initial value [34]. Guo et al. examined the mechanical properties of shale under triaxial stress conditions, observing a 13.7% and 36.9% reduction in compressive strength and elastic modulus, respectively, at 150 °C [35]. Li, using digital image correlation techniques, studied the fracture evolution of deep shale under real-time high temperatures from room temperature to 195 °C and found that both stiffness and fracture toughness of the shale increased with temperature [22].Due to limitations in experimental equipment, current research on rock mechanics under real-time high-temperature conditions has primarily been conducted at relatively low temperatures (below 300 °C). However, during in situ extraction, oil shale is subjected to real-time high temperatures of around 450 °C. The physical and mechanical properties of oil shale under the coupled effects of pyrolysis and thermal fracturing are more complex than those of conventional rocks. Therefore, further research is necessary to explore the fracture evolution of oil shale under real-time high-temperature conditions.

To explore the evolution mechanism of fracture characteristics in oil shale under real-time high-temperature conditions, this study integrates both macroscopic and microscopic approaches. At the microscopic scale, the thermal response behavior of mineral components, including inorganic minerals and organic matter, as well as the evolution of pores and fractures, were systematically analyzed under real-time high-temperature conditions. Furthermore, using a self-developed real-time high-temperature rock fracture testing system, the macroscopic fracture mechanics were investigated for prefabricated cracks propagating along the three principal directions—Arrester, Divider, and Short-Transverse—relative to the isotropic plane. The results of this study provide essential theoretical insights for the optimization and implementation of in situ oil shale pyrolysis technology.

2. Experimental Method

2.1. Sample Preparation

The oil shale samples used in the experiments were obtained from the −60 m position of the Taimu Lignite Mine in Xinjiang, China. At room temperature, the mineral composition of the samples was analyzed using polarized light microscopy and X-ray diffraction (XRD), the polarized light microscope used is a DM2700P manufactured by Leica, Germany, while the X-ray diffractometer is a Smartlab Rigaku 2019 produced by Rigaku, Japan. The results indicate that the clay minerals in the oil shale are predominantly mixed-layer illite-smectite, with smaller amounts of kaolinite, illite, and chlorite. The non-clay minerals are primarily quartz, with potassium feldspar and plagioclase also present. Organic matter is distributed in a banded pattern within the matrix, parallel to the bedding planes, as illustrated in Figure 1.

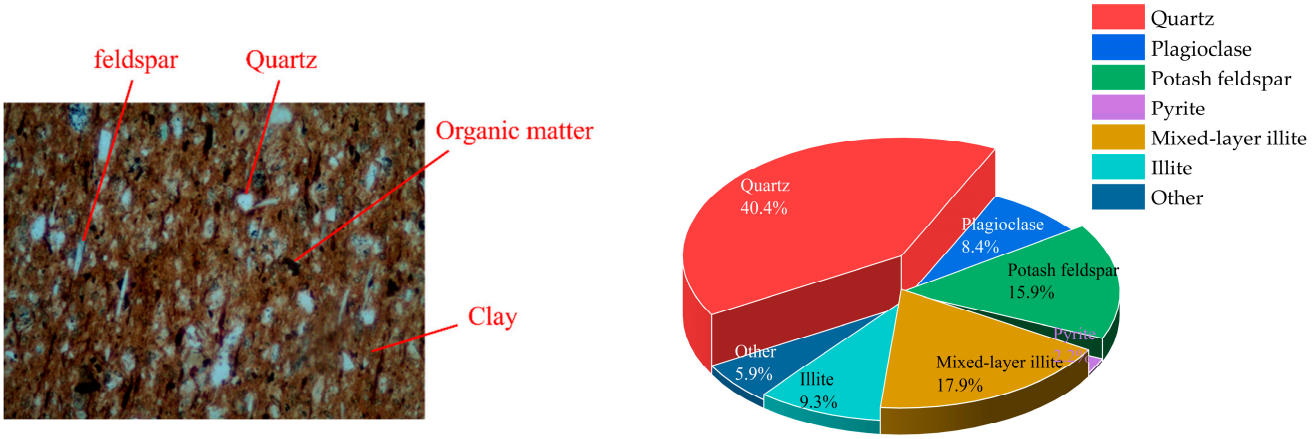

Figure 1. Polarizing microscopy images and mineral content of oil shale.

To ensure the scientific validity of the experimental results, all test samples were sourced from the same block of oil shale. The specifications of the samples used in the various experiments are as follows: (1) Powdered samples with a particle size of 200 mesh were used for the analysis of mineral composition and thermal effects under real-time high-temperature conditions; (2) cubic samples with dimensions of 4 × 3 × 1 mm were prepared for surface morphology observations; (3) cylindrical samples with dimensions of Φ8 × 16 mm were used for analyzing the microstructural evolution under thermomechanical coupling; (4) due to the presence of internal weak planes in oil shale, sample preparation posed significant challenges. Therefore, for the real-time high-temperature Mode I fracture toughness tests, the three-point bending semi-circular bend (SCB) method recommended by the International Society for Rock Mechanics (ISRM) was employed. This method offers several advantages, including ease of sample preparation, accurate measurement, and reliable test results [36]. Samples with prefabricated cracks oriented along the three principal directions relative to the bedding plane (isotropic plane) are referred to as Arrester, Divider, and Short-Transverse, as illustrated in Figure 2a. Considering the lower strength of Short-Transverse samples at high temperatures, the prefabricated crack length followed the dimensions recommended by Zhou et al. [37], with a ratio of $\beta = \tau/R = 0.2$, where the semi-circular disk radius d = 25 mm, thickness t = 20 mm, and prefabricated crack depth τ = 5 mm, as depicted in Figure 2b.

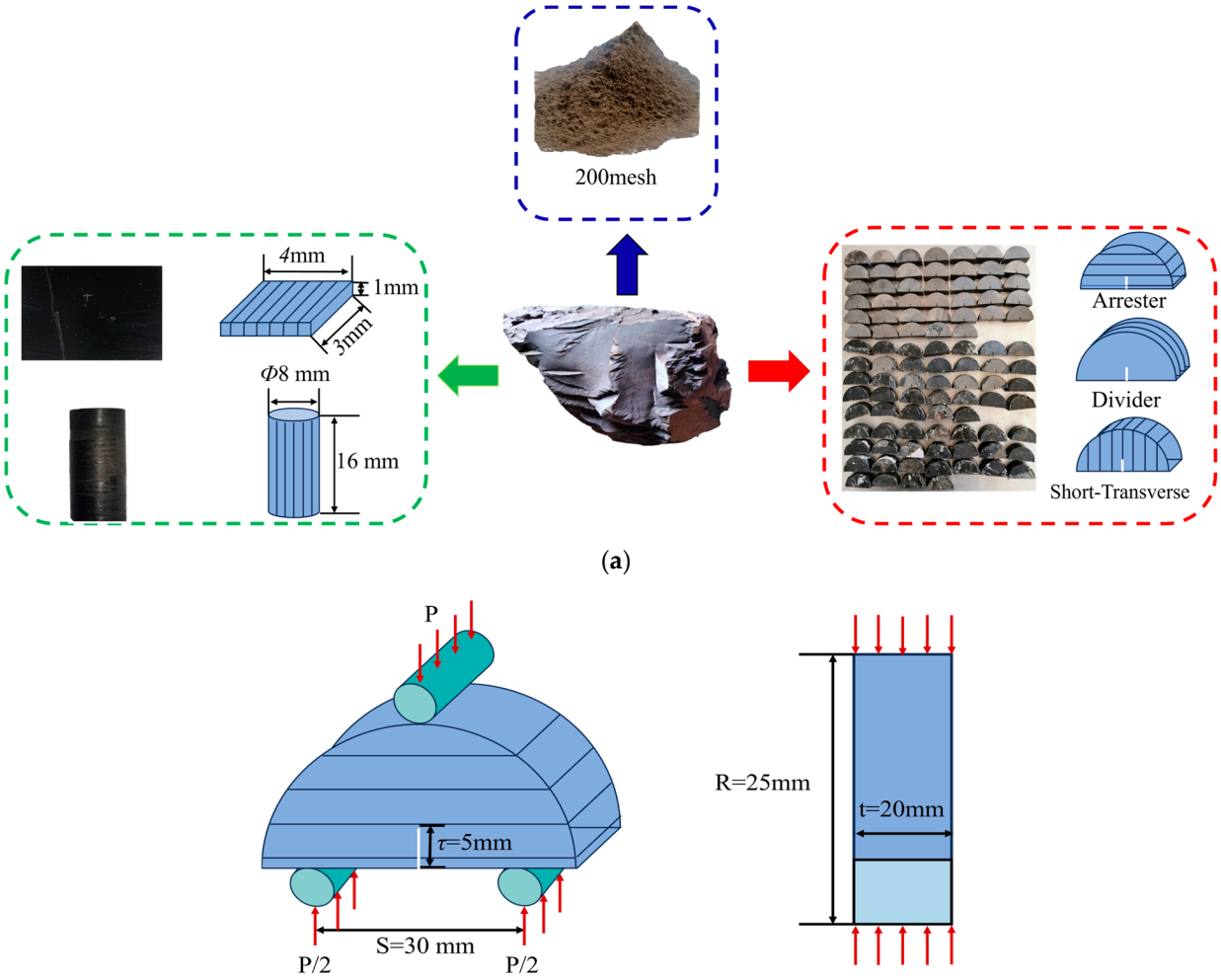

Figure 2. Schematic diagram of experimental samples and dimensions. (**a**) is a photograph of the samples processed for each experiment along with a schematic diagram of their dimensions; (**b**) is the loading parameter diagram for fracture toughness and the arrow indicates the loading direction.

2.2. Experimental Equipment and Testing Methods

2.2.1. Mineral Composition and Heat Absorption Test

The equipment used for the mineral composition analysis and differential thermal analysis of oil shale under real-time high-temperature conditions included a Smartlab Rigaku 2019 X-ray diffractometer by Rigaku, Japan, and a NETZSCH STA449 thermogravimetric differential scanning calorimeter (TG-DSC) by NETZSCH, Germany. The testing conditions for real-time high-temperature X-ray diffraction (XRD) analysis were as follows: CuKa radiation, an emission slit and scattering slit both set to 1°, a receiving slit of 0.3 mm, a scanning speed of 4°/min, a step size of 0.02 (2θ), and a scanning range from 2.6° to 70°. During the experiment, the heating rate was 0.5 °C/min, and after reaching the target temperature, the sample was maintained at a constant temperature for 0.5 h before conducting XRD analysis to ensure complete reaction of the sample. For the TG-DSC test, the heating rate was also 0.5 °C/min, with a temperature range of 20 °C to 600 °C, and argon was used as the protective gas. The equipment setup is shown in Figure 3a,b.

(**a**) (**b**)

Figure 3. Equipment for mineral composition and differential thermal analysis. (**a**) is the X-ray diffractometer; (**b**) is the thermogravimetric analyzer.

2.2.2. Microstructural Analysis

The surface morphology of oil shale after exposure to different temperatures was analyzed using a scanning electron microscope (SEM) SU8010 which is manufactured by Hitachi, Japan, with a resolution of 1.0 nm at an accelerating voltage of 15 kV. The magnification range was 20–2000× in low magnification mode and 100–800,000× in high magnification mode, as shown in Figure 4a. To ensure precise tracking of surface morphology, the samples were initially polished with argon ions, followed by laser marking prior to the experiments. Surface morphology observations after thermal treatment were conducted using a radiant heating method, with a heating rate of 0.5 °C/min. Nitrogen (N_2) was used as a protective gas during heating to prevent sample combustion. After reaching the target temperatures (100 °C, 200 °C, 300 °C, 400 °C, 500 °C, and 600 °C), the samples were held at a constant temperature for 1 h to ensure uniform internal temperature before surface morphology observations were performed.

The evolution of pore and fracture structures in oil shale under thermomechanical coupling was analyzed using a NanoVoxel-4000 3D CT scanning system, manufactured by Sanying, China, in conjunction with a self-developed thermomechanical coupling CT scanning loading device. The testing parameters were as follows: a voltage of 150 kV, a current of 100 μA, an exposure time of 2.5 s, and a pixel resolution of 9 μm/pixel. During the experiment, an axial load of 1 MPa was applied to both ends of the sample. The heating rate and constant temperature duration were consistent with those used in the surface morphology observation experiments.

Fracture toughness testing under real-time high-temperature conditions was conducted using a self-developed high-temperature rock mechanics testing system. This system has a maximum load capacity of 200 kN, with a relative error in force measurement of ±0.5%. The loading rate is adjustable between 0.001 and 500 mm/min, and the displacement resolution is 0.048 μm. The heating system can reach a maximum temperature of 800 °C, with a temperature control accuracy of ±0.1 °C, as illustrated in Figure 4.

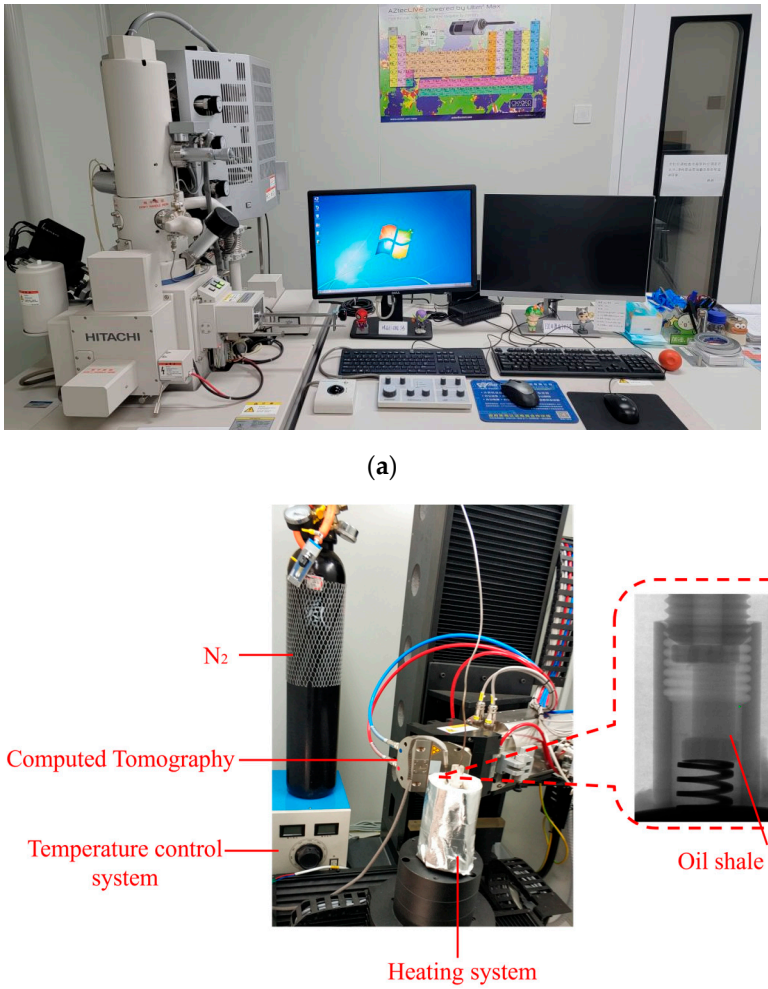

Figure 4. Microstructure testing equipment. (**a**) Scanning electron microscope SU8010; (**b**) thermomechanical coupling CT scanning device.

2.2.3. Fracture Characteristics Testing

The fracture characteristics of oil shale under real-time high-temperature conditions were assessed using a self-developed high-temperature rock fracture toughness testing system. This system features a maximum load capacity of 200 kN, with a relative error in force measurement of ±0.5%. The loading rate is adjustable from 0.001 to 500 mm/min, and the displacement resolution is 0.048 μm. The heating system can reach a maximum temperature of 800 °C, with a temperature control accuracy of ±0.1 °C. The system setup is illustrated in Figure 5.

The fracture toughness testing followed these steps: (1) The semi-circular oil shale samples were initially placed on a high-temperature heating stage, and a constant prestress of 50 N was applied. (2) The temperature control system was programmed to increase the temperature at a rate of 0.5 °C/min, sequentially reaching 100 °C, 200 °C, 300 °C, 400 °C, 500 °C, and 600 °C, while nitrogen (N_2) was introduced to maintain an oxygen-free environment in the heating chamber. After reaching the target temperature, the samples were held at a constant temperature for 2 h to ensure thermal equilibrium throughout the sample. (3) A load was applied at a rate of 0.02 mm/min until the sample fractured, and the peak load at which the prefabricated cracks propagated to failure along the Divider, Arrester, and Short-Transverse directions at different temperatures was

recorded. The fracture toughness (K_{IC}) of the SCB samples was calculated based on the ISRM-recommended method [38], as shown in the following equation.

$$\beta = \frac{\tau}{R} \tag{1}$$

$$Y' = -1.29 + 9.516\frac{S}{2R} - \left[0.47 + 16.457\left(\frac{S}{2R}\right)\right]\beta + \left[1.071 + 34.401\left(\frac{S}{2R}\right)\right]\beta^2 \tag{2}$$

$$KIC = Y'\frac{P\max\sqrt{\pi\tau}}{2Rt} \tag{3}$$

In this equation, τ is the pre-crack length (5 mm); R is the radius of the semi-circular specimen (25 mm); t is the thickness of the semi-circular specimen (20 mm); S is the distance between the centers of the two supporting rollers (30 mm); Y' is the dimensionless stress intensity factor; P_{max} is the peak load applied at the ends of the specimen (in N); and K_{IC} is the fracture toughness, expressed in MPa·mm$^{0.5}$. The value of β is set to 0.2.

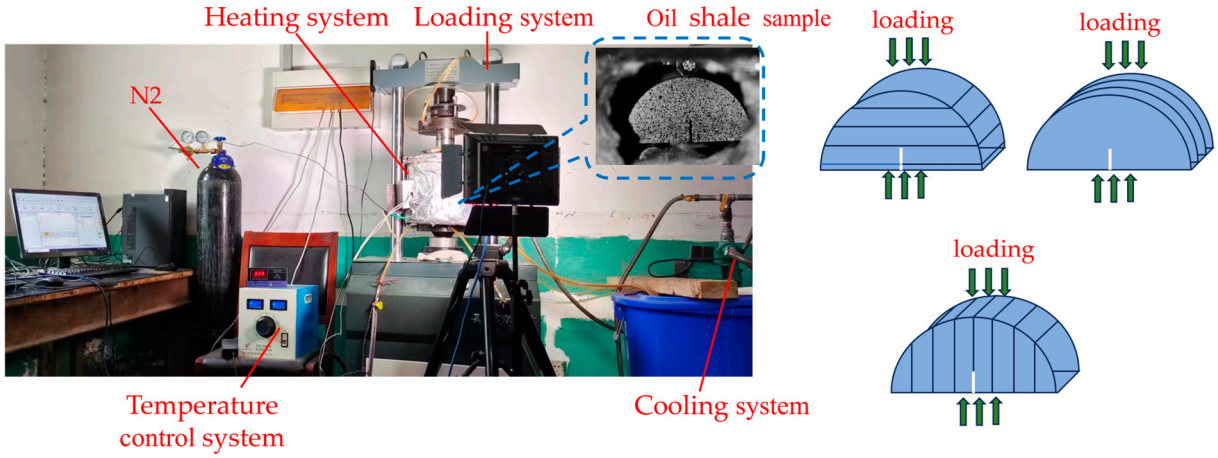

Figure 5. Schematic of the high-temperature real-time fracture toughness testing system for oil shale.

3. Results and Analysis

3.1. Mineral Composition and Differential Thermal Analysis

Figures 6 and 7 sequentially present the X-ray diffraction (XRD) curves and the differential scanning calorimetry (DSC) curves of oil shale under real-time high-temperature conditions. As shown in the figures, there is no significant change in the diffraction peaks of the mineral components in oil shale below 400 °C. The weight loss rate indicated by the thermogravimetric (TG) curve is only 3.66%, while the DSC curve shows two minor endothermic peaks at 175 °C and 370 °C. During this process, the oil shale undergoes dehydration, as well as kerogen softening and pyrolysis due to heat exposure. Water begins to evaporate at a threshold temperature of around 150 °C [39], and kerogen starts to decompose into bitumen when the temperature exceeds 350 °C [40]. Both of these processes are endothermic, resulting in a downward trend in the TG curve and the appearance of two endothermic peaks in the DSC curve.

At 400 °C, the intensity of the pyrite diffraction peak at 2θ = 31.7° begins to decrease, disappearing entirely by 500 °C. This phenomenon is attributed to the transformation of pyrite into hematite and magnetite [41]. Under the influence of 500 °C, the diffraction peaks at 2θ = 12° and 2θ = 25° also progressively decrease and disappear by 600 °C. This phenomenon is attributed to the transformation of kaolinite into metakaolinite between 450 °C and 470 °C [42]. Simultaneously, at 600 °C, the diffraction peak of the non-clay mineral quartz at 2θ = 21.8° shows a decline, likely due to the phase transition occurring at 573 °C [43]. In the temperature range of 400 °C to 600 °C, as illustrated in Figure 7, oil shale enters its primary weight loss phase, with a total weight loss of 23% by 600 °C. The DSC

curve shows an exothermic peak at 450 °C, attributed to the rapid pyrolysis of kerogen at temperatures above 400 °C, which results in the release of oil and gas products. The breaking of internal chemical bonds increases entropy and initiates endothermic reactions, leading to the observed weight loss and endothermic peaks.

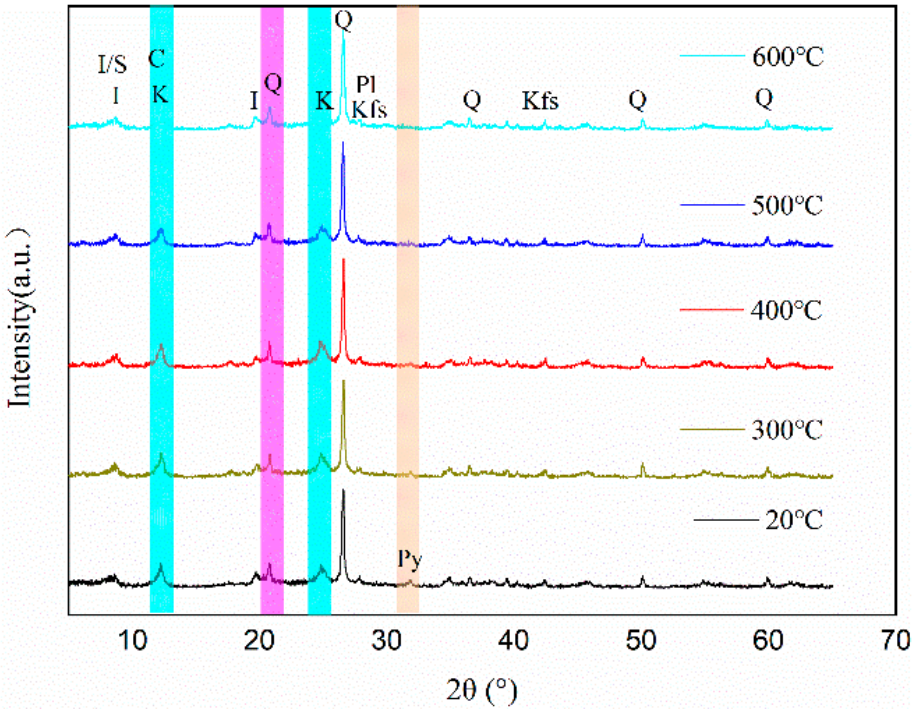

Figure 6. X-ray diffraction patterns of oil shale mineral composition at different temperatures (Q = quartz, Kfs = potash feldspar,Pl = plagioclase, K = kaolinite, I = illite, I/S = smectite,C = chlorite).

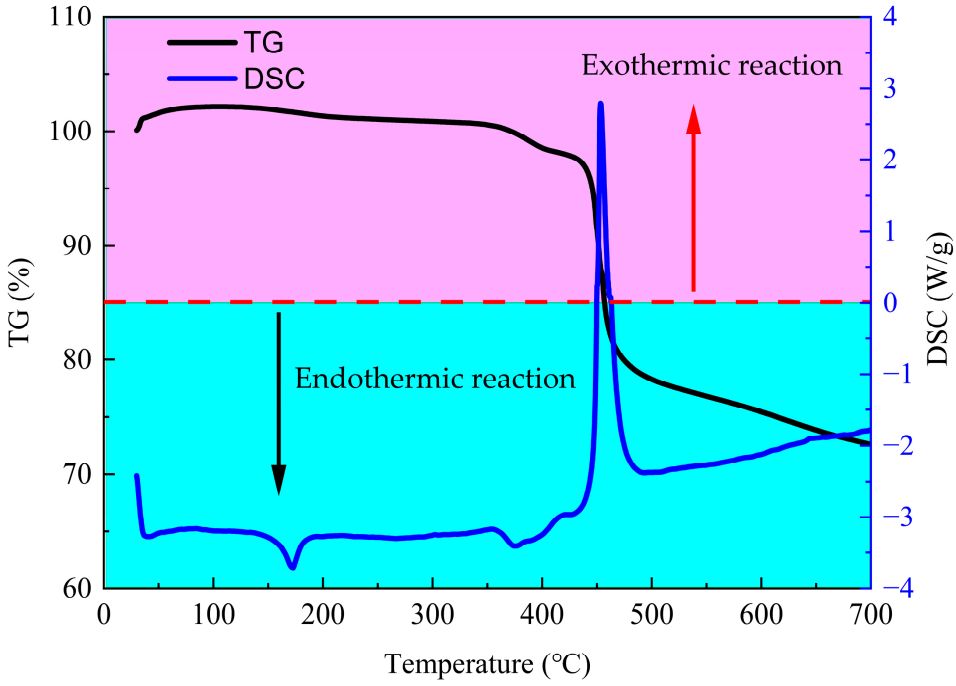

Figure 7. Thermogravimetric (TG) and differential scanning calorimetry (DSC) curves of oil shale.

3.2. Surface Morphology Analysis

Figure 8a,b illustrates the surface morphology of oil shale under natural conditions. The surface consists of clay minerals, organic matter, and various pores and fractures. Kerogen is distributed discontinuously, aligned parallel to the bedding planes within the matrix. The pores and fractures primarily include dissolution pores, intercrystalline pores and fractures, as well as organic pores and fractures. The dissolution and intercrystalline pores are approximately 50 nm in size. Intercrystalline fractures appear as flattened pores along the edges of different mineral grains, with apertures ranging from 40 to 140 nm. Organic pores are less abundant, with sizes ranging from 20 to 60 nm.

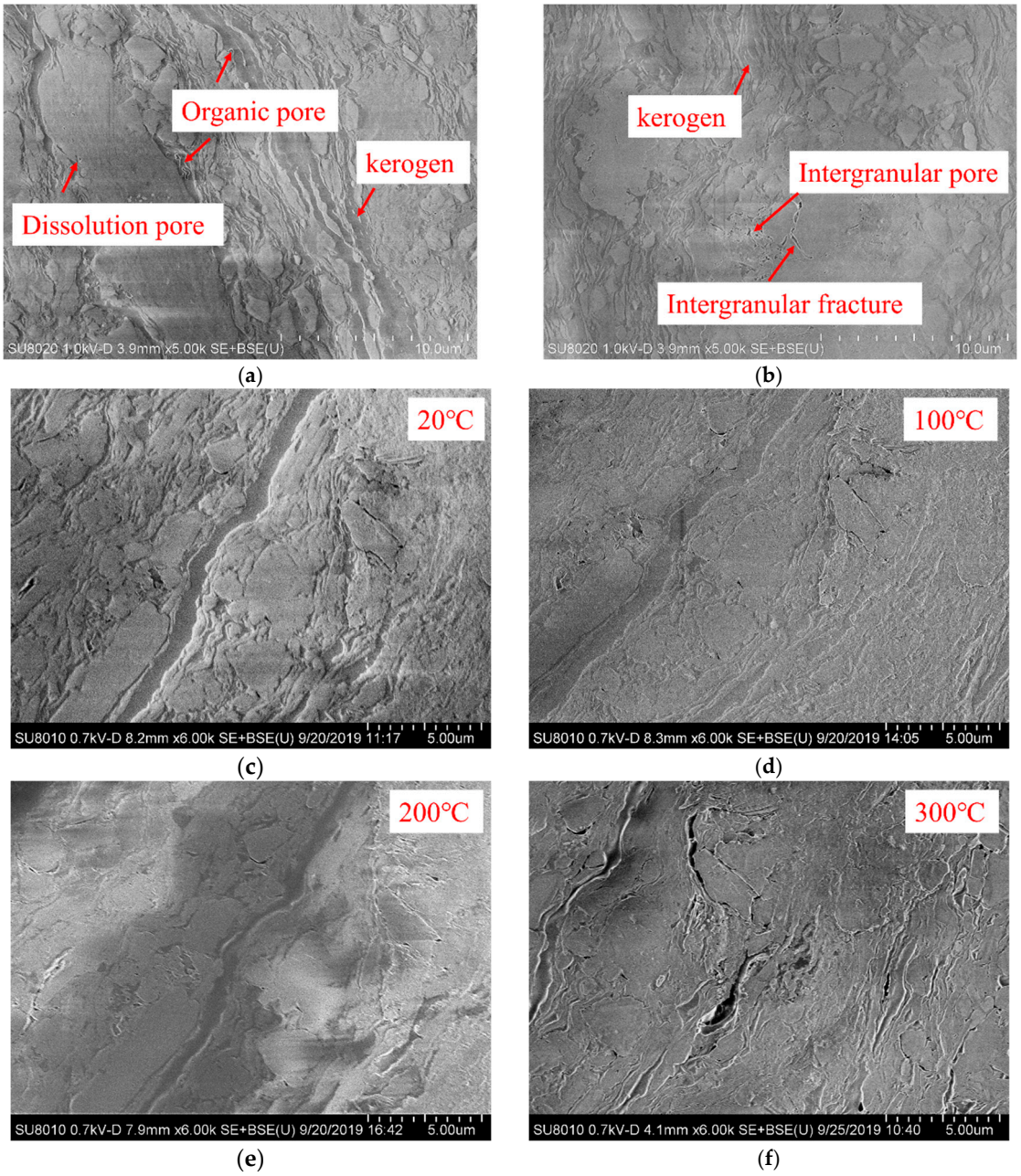

Figure 8. *Cont.*

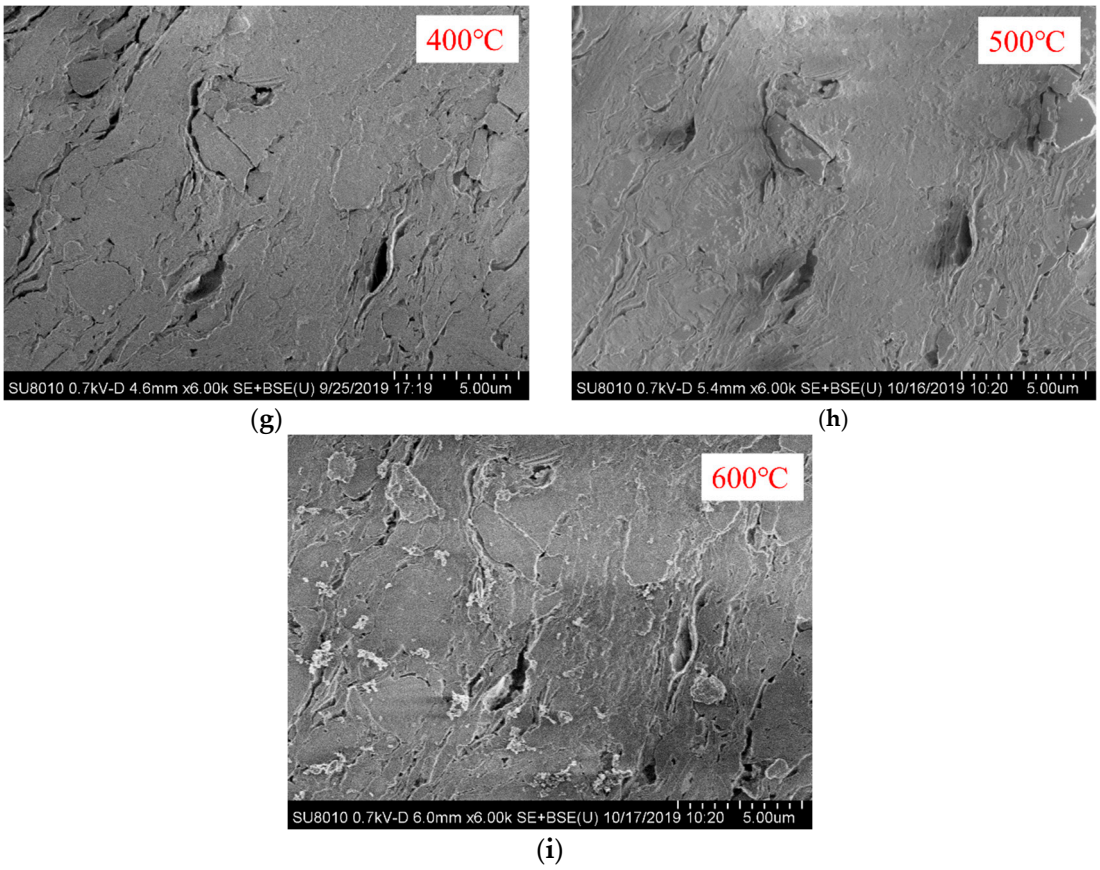

Figure 8. Surface morphology evolution of oil shale under different temperatures. (**a**,**b**) surface morphology of oil shale under natural conditions; (**c**–**i**) surface morphology of oil shale at the same location after exposure to different temperatures.

Figure 8c–i illustrates the surface morphology of oil shale at the same location after exposure to different temperatures. A comparison between Figure 8c,d reveals that after heating to 100 °C, there are no significant changes in the surface morphology. At 200 °C, the pores and fractures exhibit inward closure, with pore diameters reduced to approximately 40 nm and fracture apertures ranging from 33 to 110 nm. By 300 °C, the surface microstructure is predominantly characterized by fractures, which represents a significant change compared to the lower temperature conditions. At this stage, due to the softening of kerogen [24], the organic matter appears compressed inward, leaving behind residual fractures after its disappearance. The fracture apertures increase to between 50 and 480 nm, as illustrated in Figure 8f. At 400 °C, the surface is nearly devoid of organic matter, and the number and size of pores and fractures increase significantly, with the maximum fracture aperture reaching 1.2 μm. When the temperature is further increased to 500 °C, fracture connectivity improves, with apertures expanding to 1.6 μm. A comparison between Figure 8g,h reveals an interesting phenomenon after exposure to 500 °C: the surface matrix exhibits signs of cohesion, resulting in improved matrix integrity. As the temperature rises to 600 °C, the number, size, and connectivity of pores and fractures continue to increase, with fracture apertures reaching 1.8 μm. Additionally, vesicle-like structures of various sizes appear on the surface, which may be related to the transformation of mineral composition, as indicated in Figure 6.

3.3. Spatiotemporal Evolution Characteristics of Pores and Fractures

The distribution characteristics of fracture structures within oil shale are key factors that influence its physical and mechanical properties. Figure 9 illustrates the workflow for extracting internal pores and fractures from oil shale after CT scanning under ther-

momechanical coupling. First, three-dimensional reconstruction of the CT scan images was conducted using Avizo software-9.2. Subsequently, pore and fracture structures were identified and segmented using a threshold method to create a 3D digital model. Finally, a rendered image displaying the distribution characteristics of the pores and fractures was obtained.

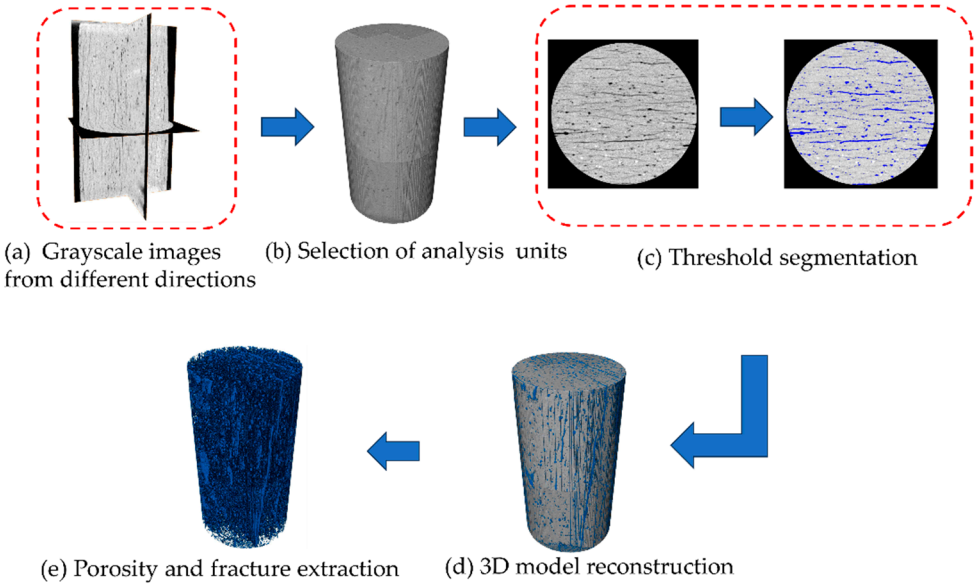

Figure 9. Diagram of the process for extracting the pore and fracture structure of oil shale.

To analyze the transformation patterns between fractures of different sizes, Chen's pore structure classification criteria were applied during the fracture extraction process [44]. Due to magnification limitations, only the spatiotemporal evolution of large and medium-sized fractures with increasing temperature was considered, as illustrated in Figure 10a,b.

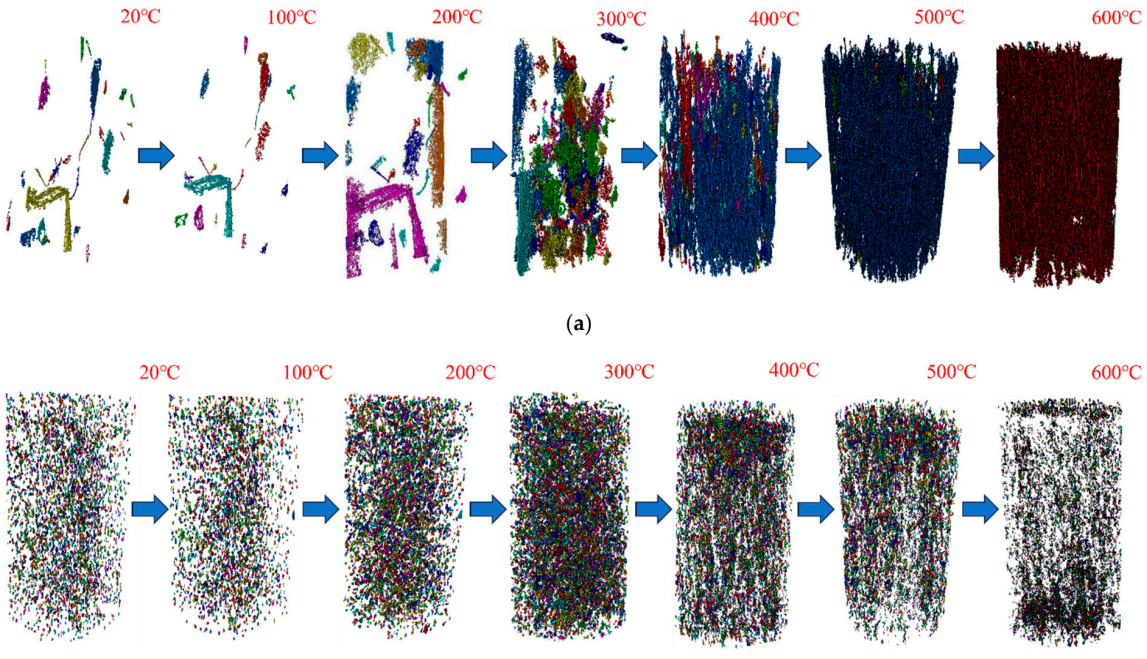

Figure 10. Spatiotemporal evolution of oil shale fractures under thermomechanical coupling: (**a**) Evolution of large fractures with temperature; (**b**) evolution of medium-sized fractures with temperature.

As illustrated in Figure 10a,b, under natural conditions, the number of large fractures in oil shale is relatively small, with most occurring sporadically and parallel to the bedding planes. In contrast, medium-sized fractures are significantly more abundant. At 100 °C, as the temperature remains relatively low and the thermal stress is minimal, neither type of fracture exhibits any significant changes, consistent with the surface morphology results observed under free-state conditions. At 200 °C, the large fractures within the oil shale begin to expand, and the number of medium-sized fractures increases significantly. This finding contrasts with the changes observed in surface morphology. The reason for this discrepancy is that when a load is applied parallel to the bedding planes, the thermal stress induced by the temperature increase leads to a rise in axial stress. Under the simultaneous influence of increasing lateral compressive stress, the bedding fractures in the oil shale extend, resulting in the observed phenomenon. At 300 °C, primary fractures continue to expand, while the number of newly formed fractures increases significantly. As discussed in Figure 8f, the key factors contributing to the expansion of primary fractures and the formation of new fractures are the residual pores left after the liquefaction and migration of organic matter, as well as the expansion behavior of rigid minerals. At 400 °C, as illustrated in Figure 10a, both the number and connectivity of fractures increase substantially, with a significant rise in the volume of large fractures, while the number of medium-sized fractures decreases. On one hand, the thermal cracking induced by the pyrolysis of organic matter into bitumen at 400 °C generates numerous fractures in the oil shale [45]. On the other hand, due to the significantly lower strength of the bedding planes compared to the matrix [46], the increasing lateral compressive stress leads to further fracture expansion. Under the combined influence of thermal cracking and lateral stress, small fractures tend to merge into larger ones, resulting in enhanced connectivity among large fractures and a reduction in the number of medium-sized fractures. As the temperature rises from 400 °C to 600 °C, Figure 10a shows a rapid increase in the number of large fractures, while Figure 10b illustrates a continuous decline in medium-sized fractures. This temperature range corresponds to the primary pyrolysis phase of kerogen, during which the thermal decomposition of organic matter exacerbates thermal cracking in the oil shale. Consequently, small fractures gradually merge with larger fractures, leading to a significant increase in both the number and connectivity of large fractures, while medium-sized fractures continue to diminish.

3.4. Load–Displacement Curves

The load–displacement curves illustrate the fracture and deformation characteristics as cracks propagate along various bedding directions, ultimately leading to failure.

At room temperature, the load–displacement curves for prefabricated cracks propagating in the Arrester, Divider, and Short-Transverse directions demonstrate typical brittle failure characteristics. As the temperature increases to 100 °C, a decrease is observed in the peak load, slope, and peak displacement, as illustrated in Figure 11a–c. This reduction can be attributed to the loss of adsorbed water between 70 °C and 100 °C, which leads to diminished cohesion [47]. When the temperature reaches 200 °C, the slope, peak load, and maximum displacement in the Arrester and Divider directions increase, while the curves in the Short-Transverse direction exhibit minimal change. The load–displacement curves for cracks propagating in the Arrester and Divider directions reflect the matrix's resistance to crack propagation, whereas those in the Short-Transverse direction indicate the relative ease of crack propagation along the bedding planes. As seen in Figures 7 and 8e, the disappearance of bound water increases friction between mineral particles [48], and the inward closure of pores in oil shale restricts crack propagation within the matrix, leading to the observed increases in the Arrester and Divider directions. However, the reduction in cohesion and the increase in bedding plane fractures at elevated temperatures facilitate crack propagation along the Short-Transverse direction, as illustrated in Figure 10a,b, thereby explaining the observed phenomenon.

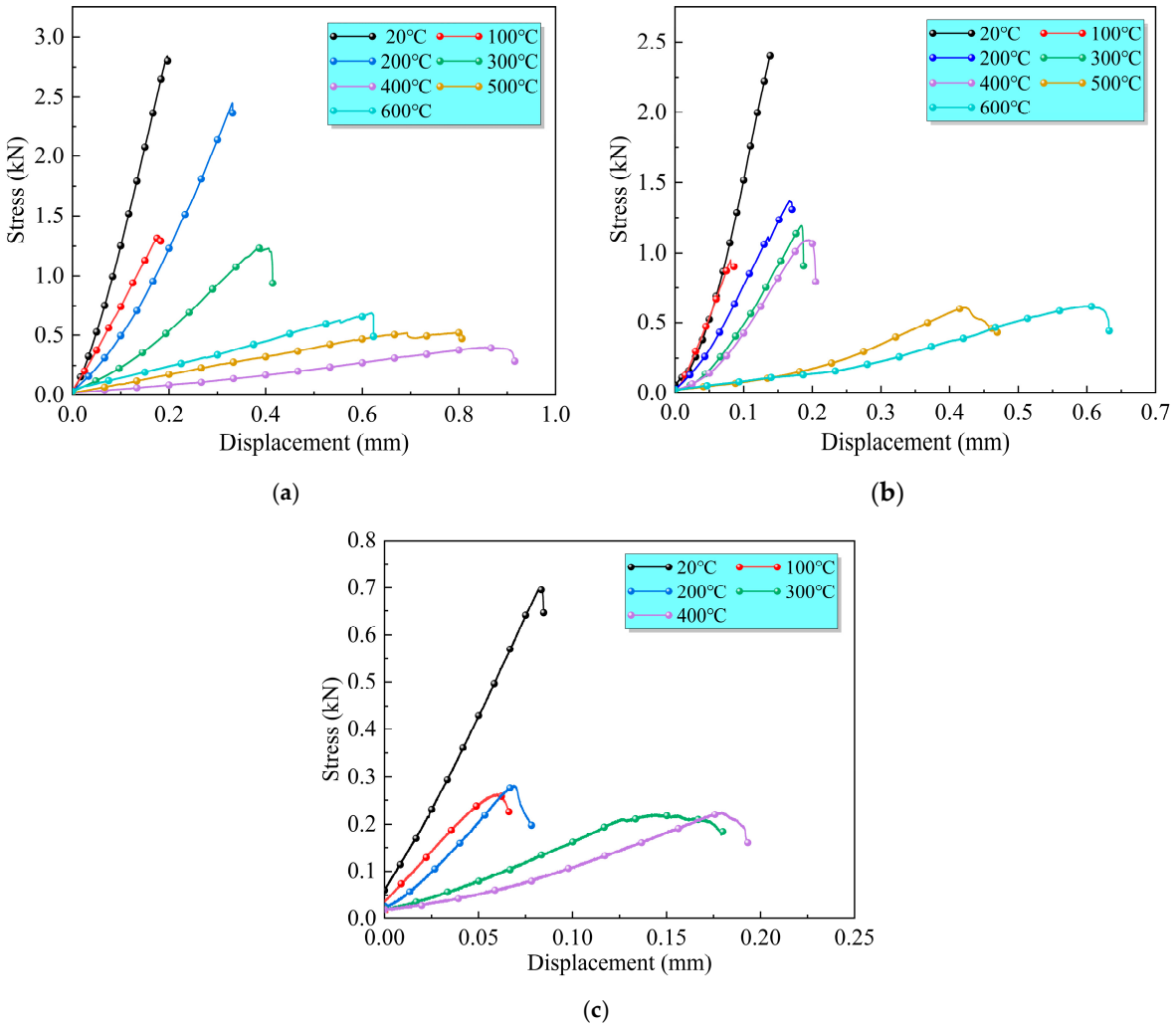

Figure 11. Load–displacement curves for crack propagation in the three principal directions relative to the bedding plane under real-time high-temperature conditions: (**a**) Arrester, (**b**) Divider, and (**c**) Short-Transverse.

Within the temperature range of 200 °C to 400 °C, as the temperature rises, the peak load and slope of the curves in Figure 11a–c decrease, while the peak displacement increases significantly. Moreover, post-peak segments emerge in the curves for all three loading directions, indicating a transition from brittle to ductile fracture in the oil shale. Since this temperature range remains below the pyrolysis threshold of kerogen, the organic matter undergoes a phase transition, cracking into bitumen and leading to matrix softening. Simultaneously, the increase in pores and fractures transforms the oil shale into a porous medium, resulting in reduced strength. Consequently, the peak load and slope continue to decrease, accompanied by a rise in peak displacement.

As the temperature rises from 400 °C to 600 °C, the behavior of the curves in Figure 11a exhibits significant differences compared to those in Figure 11b. For prefabricated cracks propagating in the Arrester direction, the curves show an increase in peak load and slope, accompanied by a decrease in displacement. In contrast, for cracks propagating in the Divider direction, the peak load and slope initially decrease before increasing, while the displacement continues to rise. Within this temperature range, the pyrolysis of organic matter generates numerous pores and fractures, resulting in a reduction in strength. Simultaneously, mineral transformation and sintering processes contribute to matrix strengthening [49,50], as shown in Figures 6 and 8g–i. When cracks propagate in the Arrester direction, the presence of bedding plane fractures restricts the extension of

prefabricated cracks and induces propagation along the bedding planes, leading to an increased peak load and slope but reduced peak displacement. In contrast, when cracks propagate in the Divider direction, they are confined to a single bedding plane. The pores and fractures generated by pyrolysis weaken the matrix, causing a decrease in peak load and slope at 500 °C. However, as the temperature rises to 600 °C, mineral transformation and sintering processes strengthen the matrix, resulting in an increase in peak load and slope.

3.5. Fracture Toughness Analysis

The fracture toughness of oil shale at various temperatures reflects its resistance to crack propagation. Figure 12a–c illustrates the variation in fracture toughness for prefabricated cracks propagating in the Arrester, Divider, and Short-Transverse directions over a temperature range of 20 °C to 600 °C. At room temperature, the fracture toughness of oil shale exhibits significant anisotropy. The fracture toughness for cracks propagating in the Arrester direction ($K_{IC\text{-}Arr}$) is the highest, at 1.1 MPa·m$^{0.5}$; for the Divider direction ($K_{IC\text{-}Div}$), it is slightly lower, at 0.91 MPa·m$^{0.5}$; and for the Short-Transverse direction ($K_{IC\text{-}Shor}$) it is the lowest, at 0.28 MPa·m$^{0.5}$.

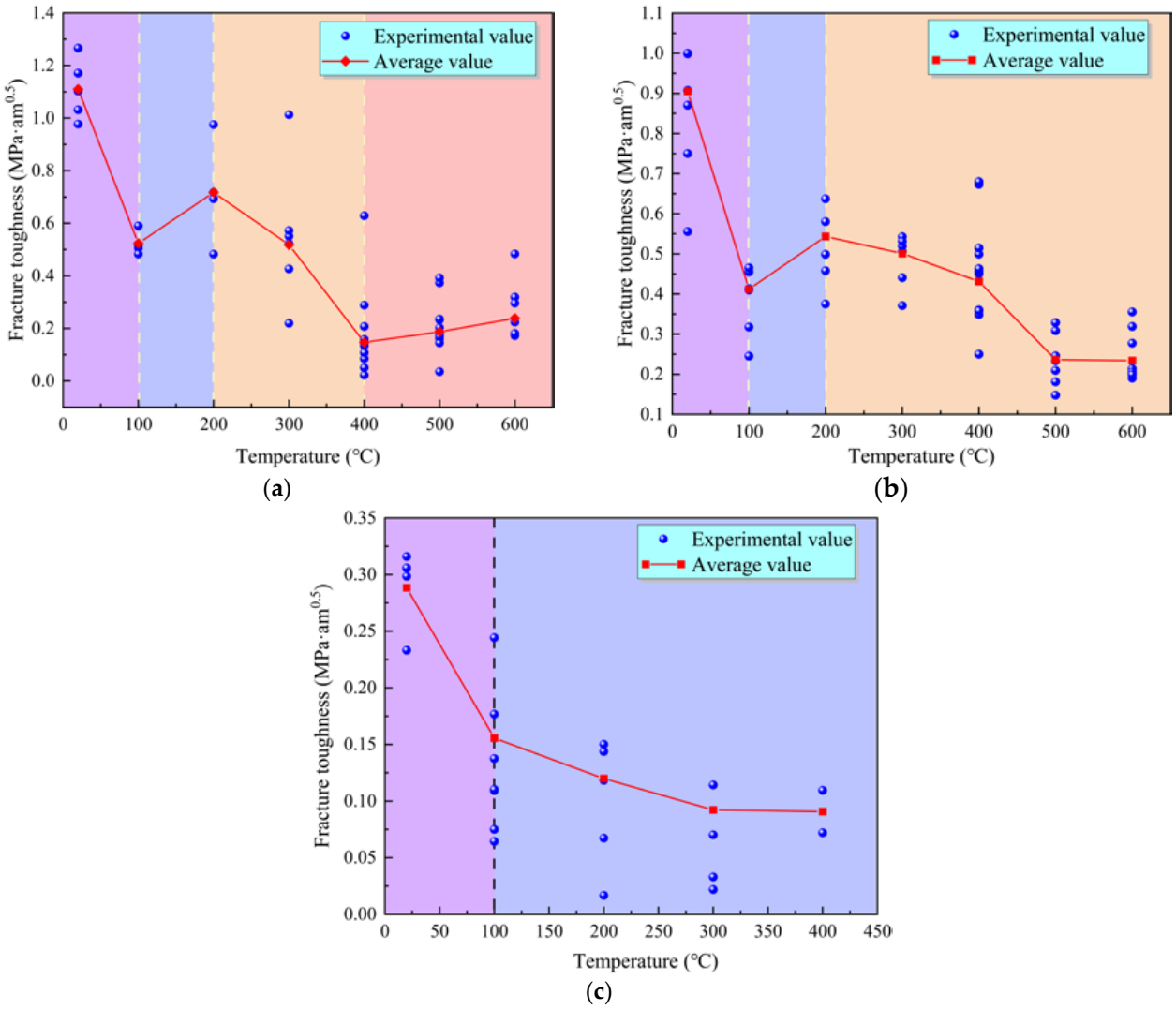

Figure 12. Fracture toughness versus temperature curves for prefabricated cracks propagating in different orientations relative to bedding under real-time high-temperature conditions: (**a**) Arrester, (**b**) Divider, and (**c**) Short-Transverse.

As the temperature increases from 20 °C to 100 °C, both $K_{IC\text{-}Arr}$ and $K_{IC\text{-}Div}$ decrease rapidly. At 100 °C, $K_{IC\text{-}Arr}$ and $K_{IC\text{-}Div}$ are 0.52 MPa·m$^{0.5}$ and 0.41 MPa·m$^{0.5}$, respectively. During this phase, the reduction in cohesion between mineral particles diminishes the oil shale's resistance to crack propagation, resulting in a decline in fracture toughness over this temperature range [51]. When the temperature rises from 100 °C to 200 °C, $K_{IC\text{-}Arr}$ and $K_{IC\text{-}Div}$ increase to 0.72 MPa·m$^{0.5}$ and 0.54 MPa·m$^{0.5}$, respectively. This behavior contrasts with the results typically observed after high-temperature treatment [52,53]. This discrepancy arises because, under real-time high-temperature conditions, fracture toughness is influenced by the combined effects of cohesion, effective stress, thermal stress, and friction between mineral particles. At this stage, the inward closure of pores restricts crack propagation, leading to an increase in fracture toughness. Conversely, after high-temperature treatment, the mechanical strength of oil shale is primarily governed by cohesion, resulting in contrasting test outcomes. In the temperature range of 200 °C to 400 °C, both $K_{IC\text{-}Arr}$ and $K_{IC\text{-}Div}$ continue to decrease as the temperature rises, reaching 0.15 MPa·m$^{0.5}$ and 0.43 0.15 MPa·m$^{0.5}$, respectively, at 400 °C. During this phase, the liquefaction of kerogen generates numerous organic fractures, as shown in Figures 8d and 10a,b, resulting in a reduction in matrix strength and a continuous decline in $K_{IC\text{-}Arr}$ and $K_{IC\text{-}Div}$.

As the temperature rises from 400 °C to 600 °C, $K_{IC\text{-}Arr}$ gradually increases to 0.238 MPa·m$^{0.5}$, while $K_{IC\text{-}Div}$ initially decreases and then increases, reaching 0.234 MPa·m$^{0.5}$ at 600 °C. By 400 °C, the bedding fracture network in the oil shale is largely developed, as depicted in Figures 8g and 10a,b. Further heating strengthens the matrix due to the transformation of clay minerals and sintering effects [43,49,54]. When cracks propagate in the Arrester direction and encounter a bedding fracture, the underlying matrix must fracture again, resulting in an increase in $K_{IC\text{-}Arr}$. Figure 6 illustrates that the primary pyrolysis of organic matter occurs between 400 °C and 550 °C. At 500 °C, the number of pores within the matrix is significantly greater than at 400 °C. Consequently, the fracture toughness $K_{IC\text{-}Div}$ continues to decrease as cracks propagate in the Divider direction. Furthermore, heating to 600 °C has minimal impact on the matrix pore structure, while the increase in matrix strength becomes the primary factor contributing to the rise in $K_{IC\text{-}Div}$.

When cracks propagate in the Short-Transverse direction, the cohesion between bedding planes is a critical factor in determining fracture toughness. At 20 °C, $K_{IC\text{-}Shor}$ is measured at 0.29 MPa·m$^{0.5}$. As the temperature rises from 20 °C to 100 °C, $K_{IC\text{-}Shor}$ decreases rapidly to 0.15 MPa·m$^{0.5}$, attributed to the reduction in bonding strength of the bedding planes caused by the loss of adsorbed water. From 100 °C to 400 °C, the $K_{IC\text{-}Shor}$ curve continues to decline, although at a significantly reduced rate. Since this temperature range does not yet reach the pyrolysis stage of organic matter, the effect of temperature on the reduction of bedding cohesion gradually diminishes, resulting in a marked decrease in the rate of reduction of $K_{IC\text{-}Shor}$.

3.6. Absorbed Energy Analysis

Under external forces, the deformation and failure of rocks are characterized by the accumulation, transformation, dissipation, and release of energy. Under real-time high-temperature conditions, the fracturing of oil shale in different directions is fundamentally driven by the expansion of internal cracks under external loading and the associated energy consumption. Therefore, investigating the energy absorption of oil shale at failure in various directions is crucial for determining relevant fracturing parameters for subsequent reservoir modification processes. The energy required for oil shale to reach failure under loading can be quantified by calculating the area beneath the load–displacement curve along the horizontal axis [12], as illustrated in Figure 13; the calculation method is provided in Equation (4).

$$U = \int_0^{S_i} P_i \cdot ds \tag{4}$$

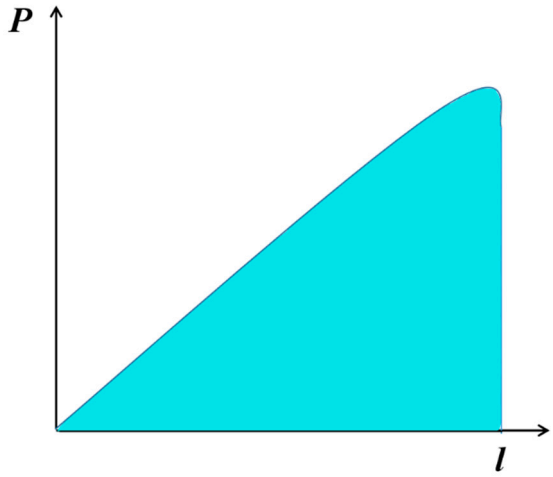

Figure 13. Calculation diagram of final absorbed energy.

In the equation, U represents the absorbed energy (in mJ); P_i denotes the load applied to the specimen at the i-th time step (in N); ds is the displacement increment between the i-th and i + 1-th time steps (in mm); and S_i is the displacement value at the i-th time step.

Figure 14 demonstrates that, at room temperature, the absorbed energy during the failure of prefabricated cracks propagating in the Arrester direction is the highest, reaching 253 mJ. As the temperature increases to 100 °C, E_{Arr} drops to 98.2 mJ, representing 39% of the absorbed energy at room temperature. This reduction is attributed to the decrease in peak load at this temperature, as depicted in Figure 11a. When the temperature rises to 200 °C, E_{Arr} increases to 281 mJ, and at 300 °C, it reaches 285 mJ, both values approximately 1.1 times the energy absorbed at room temperature. A comparative analysis of Figures 11a and 12a reveals that, although the peak load during the failure of oil shale at 200 °C and 300 °C is lower than at room temperature, deformation is greater at these higher temperatures. This suggests that, within this temperature range, the extent of deformation during failure has a more significant influence on energy absorption.

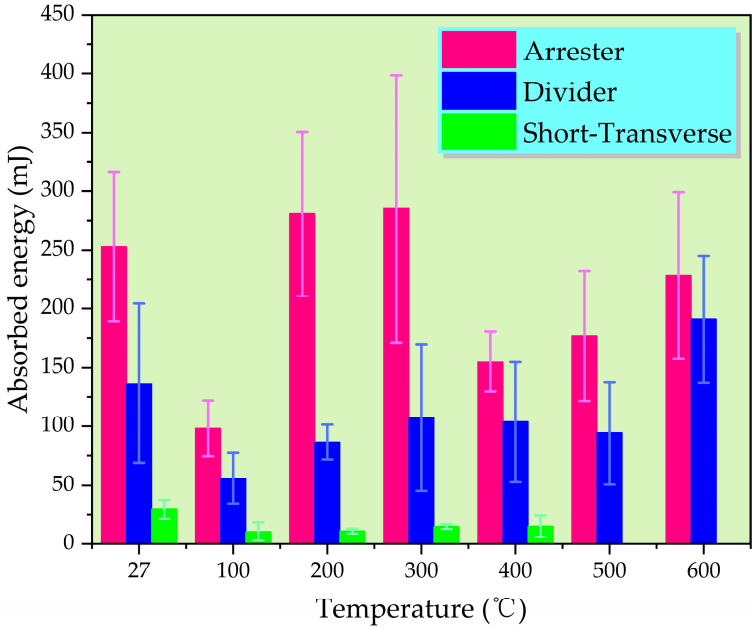

Figure 14. Variation of absorbed energy with temperature for pre-existing cracks propagating in different directions relative to layering under real-time high-temperature conditions.

At 400 °C, E_{Arr} decreases to 155 mJ, representing 61% of the energy absorbed at room temperature. Despite the peak displacement being highest at 400 °C, as depicted in Figure 11a, the substantial reduction in fracture toughness leads to a corresponding decrease in E_{Arr}. As the temperature continues to rise to 600 °C, E_{Arr} increases again, reaching 228 mJ, which corresponds to 90% of the energy absorbed at room temperature. Analysis of Figures 11a and 12a reveals that, although peak displacement continues to decrease, the increasing fracture toughness with rising temperature causes E_{Arr} to rise steadily. Thus, it is evident that after reaching 400 °C, fracture toughness becomes the key factor governing the amount of energy absorbed.

At room temperature, the absorbed energy (E_{Div}) during crack initiation and propagation along the Divider direction until failure is 136.7 mJ. Within the temperature range of 20 °C to 400 °C, the trends of E_{Div}, E_{Arr}, $K_{IC\text{-}Arr}$, and $K_{IC\text{-}Div}$, as well as the stress-strain curves under both loading conditions, are similar and thus will not be reiterated here. As the temperature increases from 400 °C to 500 °C, E_{Div} declines, in contrast to the rebound observed in E_{Arr}. Analysis of Figure 11b reveals that at 500 °C, despite an increase in peak displacement, the peak load decreases significantly, resulting in a reduction of E_{Div}. At 600 °C, both the peak load and peak displacement increase, leading to a rise in E_{Div}, reaching 191 mJ, which is 1.4 times the absorbed energy at room temperature. It can be concluded that the least energy is required at 100 °C for crack propagation to failure along both the Arrester and Divider directions. Within the temperature range of 20 °C to 200 °C, the absorbed energy during the failure of oil shale is influenced by both deformation and fracture toughness. From 200 °C to 300 °C, the absorbed energy is primarily driven by deformation. In the temperature range of 300 °C to 600 °C, for crack propagation along the Arrester direction, the absorbed energy is governed by fracture toughness. However, for crack propagation along the Divider direction, the absorbed energy is influenced by fracture toughness between 300 °C and 500 °C, while both fracture toughness and deformation contribute within the 500 °C to 600 °C range.

Under ambient temperature conditions, the absorbed energy (E_{shor}) during crack propagation along the Short-Transverse direction is the lowest, recorded at 29.68 mJ. When the temperature rises to 100 °C, E_{shor} decreases to 11 mJ, representing only 37% of the value at ambient temperature. This reduction can be attributed to decreased cohesion, which leads to a reduction in both peak load and peak displacement during crack propagation along the Short-Transverse direction, thereby resulting in a lower E_{shor}. From 100 °C to 400 °C, E_{shor} continuously increases with rising temperature, reaching 16 mJ at 400 °C, which represents 54% of the absorbed energy at ambient temperature. An analysis of Figures 8g, 10 and 11c indicates that the presence of bedding fractures reduces the peak load during crack propagation along the Short-Transverse direction, while the transition from brittleness to ductility, caused by matrix softening, increases peak displacement, thereby leading to greater energy consumption. Thus, it can be concluded that the energy required for fracturing along the Short-Transverse direction is minimized at 100 °C, whereas the transition from brittleness to ductility results in higher energy consumption for crack formation.

4. Discussion

As a typical sedimentary rock characterized by well-developed bedding planes, natural fractures, and abundant organic content, the mechanical properties of oil shale are influenced by its mineral composition, organic matter, pore and fracture network structure, fluid presence, and temperature [55,56]. In the low-temperature range (20 °C $\leq$ T $\leq$ 200 °C), the evolution of fracture characteristics in oil shale is primarily governed by various forms of moisture loss and thermal stress, which change with increasing temperature. Initially, the loss of interlayer water, occurring between 80 °C and 100 °C, reduces cohesion between the matrix and bedding planes, resulting in a rapid decrease in mechanical strength [47,57]. As the temperature rises beyond 150 °C, the closure of pores due to incompatible deformation of minerals results in the release of pore water and weakly bound water [32,58],

as evidenced in Figure 7. This phenomenon results in the hardening of clay minerals, increased friction between mineral grains, enhanced effective stress, and the inward closure of inorganic pores and fractures, as illustrated in Figure 8e, thereby strengthening the resistance of the oil shale matrix to crack propagation [59,60]. However, these factors exert minimal influence on the cohesion between bedding planes.

In the medium temperature range (200 °C < T ≤ 400 °C), kerogen begins to convert into bitumen at approximately 270 °C [61], and the formation of organic pores and fractures during this stage is a critical factor in the reduction of the mechanical properties of oil shale at 300 °C. However, the presence of liquid bitumen facilitates the transition of oil shale from brittleness to ductility, reducing the crack propagation rate, increasing deformation, and ultimately leading to an increase in absorbed energy during fracture. At a high temperature of 400 °C, the internal crystallized water in the oil shale evaporates, enhancing its fracture toughness [62]. Conversely, the formation of bitumen, the release of mixed hydrocarbon gases, and the increased porosity and connectivity between bedding fractures and matrix pores deteriorate the fracture toughness of oil shale, as illustrated in Figures 8d and 10. The negative effects on fracture toughness outweigh the positive effects of the disappearance of crystallized water, resulting in a reduction in fracture toughness in all three directions. At this temperature, fracture toughness becomes the dominant factor influencing the absorbed energy during crack propagation along the Arrester and Divider directions, leading to a decrease in E_{Arr} and E_{Div}. However, during crack propagation in the Short-Transverse direction, although thermal cracking reduces cohesion between bedding planes and decreases fracture toughness, it also generates numerous microcracks at the prefabricated crack tip, resulting in a transition from single-crack initiation to simultaneous multi-crack initiation [63]. This inevitably consumes more energy, causing E_{shor} to continue to increase.

In the high-temperature range (400 °C < T ≤ 600 °C), this phase represents the most complex and dynamic part of the entire pyrolysis process of oil shale. On one hand, at temperatures exceeding 400 °C, the decomposition of pyrite significantly increases both the number of fractures and their connectivity within the oil shale [64,65], as shown in Figures 6 and 10. On the other hand, once the temperature reaches the pyrolysis threshold of organic matter at 450 °C, rapid endothermic reactions occur, resulting in a significant increase in mass loss rate and the generation of substantial amounts of mixed hydrocarbon gases. This triggers intense thermal cracking, initiating the formation of nanoscale and microscale pore and fracture systems within the oil shale matrix [3], as illustrated in Figure 8h. Given that the primary pyrolysis of kerogen occurs between 450 °C and 550 °C, temperatures exceeding 500 °C further intensify the pyrolysis process, resulting in the interconnection of pores and fractures of varying sizes into larger fracture structures, as depicted in Figure 10, which ultimately leads to further degradation of the mechanical properties of oil shale. The dehydroxylation of clay minerals, such as kaolinite, increases the plasticity of oil shale. At 600 °C, high-temperature sintering of clay minerals enhances the mechanical strength of the matrix [64]. When cracks propagate in the Arrester direction, the presence of bedding fractures, combined with increased matrix strength along the bedding plane, restricts the main crack propagation, resulting in an increase in fracture toughness and absorbed energy at failure [63]. In contrast, when cracks propagate in the Divider direction, crack growth remains confined within the same bedding layer. The presence of pores and fractures contributes to a continued decline in fracture characteristics at 500 °C in this direction. However, when the temperature increases to 600 °C, the enhanced matrix strength leads to an increase in both $K_{\mathrm{IC-Div}}$ and E_{Div}.

5. Conclusions

To elucidate the evolution mechanisms governing the fracture behavior of oil shale under real-time high-temperature conditions, this study employed an integrated macro- and microscale analytical approach. Using field emission scanning electron microscopy, a thermally coupled CT scanning system, and a custom-developed real-time high-temperature

rock fracture toughness testing apparatus, a comprehensive investigation was conducted into the spatiotemporal evolution of the microstructural characteristics of Xinjiang oil shale. Furthermore, the fracture behavior during crack propagation in the Arrester, Divider, and Short-Transverse orientations was systematically examined. The principal findings are summarized as follows:

(1) Under natural conditions, the internal pores and fractures of oil shale are predominantly inorganic, with only a small proportion of organic pores present. Below 200 °C, the effect of temperature on pores and fractures is minimal. At 200 °C, inorganic pores begin to close inward due to thermal expansion, while inorganic fractures expand along the bedding planes. At 300 °C, the number and connectivity of organic pores and fractures increase as kerogen undergoes liquefaction. When the temperature reaches 400 °C, both the size and connectivity of inorganic and organic pores and fractures increase significantly. Beyond 500 °C, the oil shale matrix exhibits adhesion between clay minerals, and at 600 °C, vesicular structures emerge.

(2) Below 300 °C, oil shale exhibits brittle fracture characteristics, while beyond 300 °C, a transition from brittle to ductile fracture occurs. Within the temperature range of 20 °C to 400 °C, except for a sudden drop in peak load at 100 °C, the peak load, slope, and peak displacement of the load–displacement curve consistently decrease with increasing temperature. As the temperature rises from 400 °C to 600 °C, the peak load and slope of the curve during crack propagation in the Arrester direction gradually increase, whereas the peak displacement decreases. In contrast, during crack propagation in the Divider direction, the peak load and slope decrease, while the peak displacement increases.

(3) At ambient temperature, the fracture toughness of oil shale exhibits significant anisotropy. Fracture toughness is highest when prefabricated cracks propagate in the Arrester direction, followed by the Divider direction, and is lowest in the Short-Transverse direction. Within the temperature range of 20 °C to 400 °C, fracture toughness along the Arrester and Divider directions generally shows a declining trend with increasing temperature, but a rebound is observed as the temperature rises from 100 °C to 200 °C. Once the temperature reaches 400 °C, further heating leads to an increase in fracture toughness in the Arrester direction, whereas in the Divider direction, fracture toughness initially decreases and then gradually increases. When cracks propagate in the Short-Transverse direction, the fracture toughness of oil shale continuously decreases with increasing temperature from 20 °C to 400 °C.

(4) At 100 °C, the energy required for crack propagation to failure in oil shale is minimal. Beyond 100 °C, the absorbed energy required for failure increases steadily with temperature when prefabricated cracks propagate in the Divider and Short-Transverse directions. Within the temperature range of 20 °C to 600 °C, the absorbed energy required for crack propagation to failure along the Arrester direction exhibits a 'W'-shaped distribution, with troughs observed at 100 °C and 400 °C.

Author Contributions: Conceptualization, methodology, validation, writing—review and editing, and funding acquisition, S.Y.; data curation and investigation, Q.Z.; software, D.Y. All authors have read and agreed to the published version of the manuscript.

Funding: This work was supported by Taiyuan University of science technology Scientific Research Initial Funding (Grant No. 20222028 and 20222036), Fundamental Research Program of Shanxi Province (Grant No. 202203021212311) and Scientific and Technological Innovation Programs of Higher Education Institutions in Shanxi (Grant No. 2022L307).

Data Availability Statement: The original contributions presented in the study are included in the article, further inquiries can be directed to the corresponding author.

Conflicts of Interest: The authors declare no conflicts of interest.

References

1. Han, X.; Kulaots, I.; Jiang, X.; Suuberg, E.M. Review of Oil Shale Semicoke and Its Combustion Utilization. *Fuel* **2014**, *126*, 143–161. [CrossRef]
2. Zhao, X.; Zhang, X.; Liu, Z.; Lu, Z.; Liu, Q. Organic Matter in Yilan Oil Shale: Characterization and Pyrolysis with or without Inorganic Minerals. *Energy Fuels* **2017**, *31*, 3784–3792. [CrossRef]
3. Kang, Z.; Zhao, Y.; Yang, D. Review of Oil Shale In-Situ Conversion Technology. *Appl. Energy* **2020**, *269*, 115121. [CrossRef]
4. Jiang, X.M.; Han, X.X.; Cui, Z.G. New Technology for the Comprehensive Utilization of Chinese Oil Shale Resources. *Energy* **2007**, *32*, 772–777. [CrossRef]
5. Liu, Z.; Li, H.; Liu, S.; Chen, J.; Zhang, Z.; Li, X.; Zhang, A.; Yuan, W.; Gao, X. Thermodynamics Fundamentals and Energy Efficiency for the Separation and High-Valued Utilization of Fischer–Tropsch Heavy Oil. *Int. J. Coal Sci. Technol.* **2022**, *9*, 57. [CrossRef]
6. Guo, W.; Deng, S.; Sun, Y. Recent Advances on Shale Oil and Gas Exploration and Development Technologies. *Adv. Geo-Energy Res.* **2024**, *11*, 81–87. [CrossRef]
7. Song, X.; Zhang, C.; Shi, Y.; Li, G. Production Performance of Oil Shale In-Situ Conversion with Multilateral Wells. *Energy* **2019**, *189*, 116145. [CrossRef]
8. Gu, J.; Deng, S.; Fu, H.; Yu, D.; Tang, W.; Sun, Y.; Guo, W.; Shi, W. Pyrolysis Characteristics and Evolution of the Organics in Nong'an Oil Shale Lump during Sub-Critical Water Extraction. *Fuel* **2024**, *364*, 131064. [CrossRef]
9. Gu, J.; Deng, S.; Sun, Y.; Guo, W.; Chen, H.; Shi, B. Pyrolysis Behavior and Pyrolysate Characteristics of Huadian Oil Shale Kerogen Catalyzed by Nickel-Modified Montmorillonite. *Adv. Geo-Energy Res.* **2024**, *11*, 168–180. [CrossRef]
10. Chang, X.; Wang, X.; Yang, C.; Guo, Y.; Wan, Y. Experimental Investigation on Mode I Fracture Characteristics of Longmaxi Formation Shale after Cyclic Thermal Shock and High-Temperature Acid Etching Treatments. *Eng. Fract. Mech.* **2024**, *295*, 109762. [CrossRef]
11. Bennour, Z.; Ishida, T.; Nagaya, Y.; Chen, Y.; Nara, Y.; Chen, Q.; Sekine, K.; Nagano, Y. Crack Extension in Hydraulic Fracturing of Shale Cores Using Viscous Oil, Water, and Liquid Carbon Dioxide. *Rock Mech. Rock Eng.* **2015**, *48*, 1463–1473. [CrossRef]
12. Feng, G.; Kang, Y.; Wang, X.; Hu, Y.; Li, X. Investigation on the Failure Characteristics and Fracture Classification of Shale Under Brazilian Test Conditions. *Rock Mech. Rock Eng.* **2020**, *53*, 3325–3340. [CrossRef]
13. Zhu, D.; Yu, B.; Wang, D.; Zhang, Y. Fusion of Finite Element and Machine Learning Methods to Predict Rock Shear Strength Parameters. *J. Geophys. Eng.* **2024**, *21*, 1183–1193. [CrossRef]
14. Islam, M.A.; Skalle, P. An Experimental Investigation of Shale Mechanical Properties through Drained and Undrained Test Mechanisms. *Rock Mech. Rock Eng.* **2013**, *46*, 1391–1413. [CrossRef]
15. Li, C.; Xie, H.; Wang, J. Anisotropic Characteristics of Crack Initiation and Crack Damage Thresholds for Shale. *Int. J. Rock Mech. Min. Sci.* **2020**, *126*, 104178. [CrossRef]
16. Habib, K.M.; Vennes, I.; Mitri, H. Laboratory Investigation into the Use of Soundless Chemical Demolitions Agents for the Breakage of Hard Rock. *Int. J. Coal Sci. Technol.* **2022**, *9*, 70. [CrossRef]
17. Shi, X.; Zhao, Y.; Danesh, N.N.; Zhang, X.; Tang, T. Role of Bedding Plane in the Relationship between Mode-I Fracture Toughness and Tensile Strength of Shale. *Bull. Eng. Geol. Environ.* **2022**, *81*, 81. [CrossRef]
18. Xiong, J.; Liu, K.; Liang, L.; Liu, X.; Zhang, C. Investigation of Influence Factors of the Fracture Toughness of Shale: A Case Study of the Longmaxi Formation Shale in Sichuan Basin, China. *Geotech. Geol. Eng.* **2019**, *37*, 2927–2934. [CrossRef]
19. Pérez-Rey, I.; Muñoz-Ibáñez, A.; González-Fernández, M.A.; Muñiz-Menéndez, M.; Herbón Penabad, M.; Estévez-Ventosa, X.; Delgado, J.; Alejano, L.R. Size Effects on the Tensile Strength and Fracture Toughness of Granitic Rock in Different Tests. *J. Rock Mech. Geotech. Eng.* **2023**, *15*, 2179–2192. [CrossRef]
20. Shi, X.; Yao, W.; Liu, D.; Xia, K.; Tang, T.; Shi, Y. Experimental Study of the Dynamic Fracture Toughness of Anisotropic Black Shale Using Notched Semi-Circular Bend Specimens. *Eng. Fract. Mech.* **2019**, *205*, 136–151. [CrossRef]
21. Zhou, Q.; Xie, H.P.; Zhu, Z.M.; He, R.; Lu, H.J.; Fan, Z.D.; Nie, X.F.; Ren, L. Fracture Toughness Anisotropy in Shale Under Deep In Situ Stress Conditions. *Rock Mech. Rock Eng.* **2023**, *56*, 7535–7555. [CrossRef]
22. Li, J.; Wang, S.; Dong, K.; Meng, S.; Lu, Q.; Li, Z. Effects of In-Situ Temperature in Deep Reservoirs on Shale Fracture Properties. *Energy Rep.* **2023**, *9*, 73–83. [CrossRef]
23. Peng, K.; Lv, H.; Zou, Q.; Wen, Z.; Zhang, Y. Evolutionary Characteristics of Mode-I Fracture Toughness and Fracture Energy in Granite from Different Burial Depths under High-Temperature Effect. *Eng. Fract. Mech.* **2020**, *239*, 107306. [CrossRef]
24. Yang, S.; Yang, D.; Kang, Z. Experimental Investigation of the Anisotropic Evolution of Tensile Strength of Oil Shale Under Real-Time High-Temperature Conditions. *Nat. Resour. Res.* **2021**, *30*, 2513–2528. [CrossRef]
25. Sundberg, J.; Back, P.E.; Christiansson, R.; Hökmark, H.; Ländell, M.; Wrafter, J. Modelling of Thermal Rock Mass Properties at the Potential Sites of a Swedish Nuclear Waste Repository. *Int. J. Rock Mech. Min. Sci.* **2009**, *46*, 1042–1054. [CrossRef]
26. Zheng, D.; Miska, S.; Ozbayoglu, E.; Zhang, J. Combined Experimental and Well Log Study of Anisotropic Strength of Shale. In Proceedings of the SPE Annual Technical Conference and Exhibition, San Antonio, TX, USA, 16–18 October 2023.
27. Hu, Y.; Hu, Y.; Zhao, G.; Jin, P.; Zhao, Z.; Li, C. Experimental Investigation of the Relationships Among P-Wave Velocity, Tensile Strength, and Mode-I Fracture Toughness of Granite After High-Temperature Treatment. *Nat. Resour. Res.* **2022**, *31*, 801–816. [CrossRef]

28. Zejin, Y.; Zhang, C. Mode I Fracture Toughness Test and Fractal Character of Fracture Trajectory of Red Sandstone under Real-Time High Temperature. *Adv. Mater. Sci. Eng.* **2019**, *2019*, 5083947. [CrossRef]
29. Guo, Q.; Su, H.; Liu, J.; Yin, Q.; Jing, H.; Yu, L. An Experimental Study on the Fracture Behaviors of Marble Specimens Subjected to High Temperature Treatment. *Eng. Fract. Mech.* **2020**, *225*, 106862. [CrossRef]
30. Suo, Y.; Zhao, Y.J.; Fu, X.F.; He, W.Y.; Pan, Z.J. Mixed-Mode Fracture Behavior in Deep Shale Reservoirs under Different Loading Rates and Temperatures. *Pet. Sci.* **2023**, *20*, 3037–3047. [CrossRef]
31. Kang, P.; Hong, L.; Fazhi, Y.; Quanle, Z.; Xiao, S.; Zhaopeng, L. Effects of Temperature on Mechanical Properties of Granite under Different Fracture Modes. *Eng. Fract. Mech.* **2020**, *226*, 106838. [CrossRef]
32. Guo, Y.; Li, X.; Huang, L. Changes in Thermophysical and Thermomechanical Properties of Thermally Treated Anisotropic Shale after Water Cooling. *Fuel* **2022**, *327*, 125241. [CrossRef]
33. Funatsu, T.; Kuruppu, M.; Matsui, K. Effects of Temperature and Confining Pressure on Mixed-Mode (I-II) and Mode II Fracture Toughness of Kimachi Sandstone. *Int. J. Rock Mech. Min. Sci.* **2014**, *67*, 1–8. [CrossRef]
34. Closmann, P.J.; Bradley, W.B. Effect of Temperature on Tensile and Compressive Strengths and Young's Modulus of Oil Shale. *Soc. Pet. Eng. AIME J.* **1979**, *19*, 301–312. [CrossRef]
35. Guo, W.; Guo, Y.; Cai, Z.; Yang, H.; Wang, L.; Yang, C.; Zhao, G.; Bi, Z. Mechanical Behavior and Constitutive Model of Shale under Real-Time High Temperature and High Stress Conditions. *J. Pet. Explor. Prod. Technol.* **2023**, *13*, 827–841. [CrossRef]
36. Mahdavi, E.; Aliha, M.R.M.; Bahrami, B.; Ayatollahi, M.R. Comprehensive Data for Stress Intensity Factor and Critical Crack Length in Chevron Notched Semi-Circular Bend Specimen Subjected to Tensile Type Fracture Mode. *Theor. Appl. Fract. Mech.* **2020**, *106*, 102466. [CrossRef]
37. Zhou, Y.X.; Xia, K.W.; Li, X.B.; Li, H.B.; Ma, G.W.; Zhao, J.; Zhou, Z.L.; Dai, F. Suggested Methods for Determining the Dynamic Strength Parameters and Mode-I Fracture Toughness of Rock Materials. In *The ISRM Suggested Methods for Rock Characterization, Testing and Monitoring: 2007–2014*; Ulusay, R., Ed.; Springer International Publishing: Cham, Switzerland, 2015; pp. 35–44, ISBN 978-3-319-07713-0.
38. Kuruppu, M.D.; Obara, Y.; Ayatollahi, M.R.; Chong, K.P.; Funatsu, T. ISRM-Suggested Method for Determining the Mode i Static Fracture Toughness Using Semi-Circular Bend Specimen. *Rock Mech. Rock Eng.* **2014**, *47*, 267–274. [CrossRef]
39. McCAIG, A.M. Fluid-rock Interaction in Some Shear Zones from the Pyrenees. *J. Metamorph. Geol.* **1984**, *2*, 129–141. [CrossRef]
40. Chang, Z.; Chu, M.; Zhang, C.; Bai, S.; Lin, H.; Ma, L. Influence of Inherent Mineral Matrix on the Product Yield and Characterization from Huadian Oil Shale Pyrolysis. *J. Anal. Appl. Pyrolysis* **2018**, *130*, 269–276. [CrossRef]
41. Eymery, J.P.; Ylli, F. Study of a Mechanochemical Transformation in Iron Pyrite. *J. Alloys Compd.* **2000**, *298*, 306–309. [CrossRef]
42. Liu, J.; Xue, Y.; Zhang, Q.; Yao, K.; Liang, X.; Wang, S. Micro-Cracking Behavior of Shale Matrix during Thermal Recovery: Insights from Phase-Field Modeling. *Eng. Fract. Mech.* **2020**, *239*, 107301. [CrossRef]
43. Heuze, F.E. High-Temperature Mechanical, Physical and Thermal Properties of Granitic Rocks—A Review. *Int. J. Rock Mech. Min. Sci.* **1983**, *20*, 3–10. [CrossRef]
44. Chen, S.; Zhu, Y.; Li, W.; Wang, H. Influence of Magma Intrusion on Gas Outburst in a Low Rank Coal Mine. *Int. J. Min. Sci. Technol.* **2012**, *22*, 259–266. [CrossRef]
45. Bai, F.; Sun, Y.; Liu, Y.; Guo, M. Evaluation of the Porous Structure of Huadian Oil Shale during Pyrolysis Using Multiple Approaches. *Fuel* **2017**, *187*, 1–8. [CrossRef]
46. Heng, S.; Guo, Y.; Yang, C.; Daemen, J.J.K.; Li, Z. Experimental and Theoretical Study of the Anisotropic Properties of Shale. *Int. J. Rock Mech. Min. Sci.* **2015**, *74*, 58–68. [CrossRef]
47. Yilmaz, G. The Effects of Temperature on the Characteristics of Kaolinite and Bentonite. *Sci. Res. Essays* **2011**, *6*, 1928–1939. [CrossRef]
48. Funatsu, T.; Seto, M.; Shimada, H.; Matsui, K.; Kuruppu, M. Combined Effects of Increasing Temperature and Confining Pressure on the Fracture Toughness of Clay Bearing Rocks. *Int. J. Rock Mech. Min. Sci.* **2004**, *41*, 927–938. [CrossRef]
49. Ip, K.H.; Stuart, B.H.; Thomas, P.S.; Ray, A.S. Thermal Characterization of the Clay Binder of Heritage Sydney Sandstones. *J. Therm. Anal. Calorim.* **2008**, *92*, 97–100. [CrossRef]
50. Pytte, A.M.; Reynolds, R.C. The Thermal Transformation of Smectite to Illite. In *Thermal History of Sedimentary Basins: Methods and Case Histories*; Springer: New York, NY, USA, 1989.
51. Saif, T.; Lin, Q.; Gao, Y.; Al-Khulaifi, Y.; Marone, F.; Hollis, D.; Blunt, M.J.; Bijeljic, B. 4D in Situ Synchrotron X-Ray Tomographic Microscopy and Laser-Based Heating Study of Oil Shale Pyrolysis. *Appl. Energy* **2019**, *235*, 1468–1475. [CrossRef]
52. Vishal, V.; Rizwan, M.; Mahanta, B.; Pradhan, S.P.; Singh, T.N. Temperature Effect on the Mechanical Behavior of Shale: Implication for Shale Gas Production. *Geosyst. Geoenviron.* **2022**, *1*, 100078. [CrossRef]
53. Feng, G.; Kang, Y.; Meng, T.; Hu, Y.; Li, X. The Influence of Temperature on Mode I Fracture Toughness and Fracture Characteristics of Sandstone. *Rock Mech. Rock Eng.* **2017**, *50*, 2007–2019. [CrossRef]
54. Yang, S.; Zhang, Q.; Yang, D.; Wang, L. Research on the Mechanism of Evolution of Mechanical Anisotropy during the Progressive Failure of Oil Shale under Real-Time High-Temperature Conditions. *Energy* **2024**, *17*, 4004. [CrossRef]
55. Nottenburg, R.N.; Rajeshwar, K.; Rosenvoid, R.J.; Dubow, J.B. Temperature and Stress Dependence of Electrical and Mechanical Properties of Green River Oil Shale. *Fuel* **1979**, *58*, 144–148. [CrossRef]

56. Mokhtari, M.; Alqahtani, A.A.; Tutuncu, A.N. Impacts of Stress, Natural and Induced Fractures on Mechanical Properties of Organic-Rich Shales. In Proceedings of the Unconventional Resources Technology Conference 2013, URTC 2013, Denver, CO, USA, 12–14 August 2013.
57. Yang, G.; Liu, J.; Li, X.; Bi, J. Effect of Temperature on Shale Strength under Dynamic Impact Loading. *Arab. J. Geosci.* **2020**, *13*, 432. [CrossRef]
58. Rao, Q.-H.; Wang, Z.; Xie, H.-F.; Qiang, X. Experimental Study of Mechanical Properties of Sandstone at High Temperature. *J. Cent. South Univ. Technol.* **2007**, *14* (Suppl. S1), 478–483. [CrossRef]
59. Han, S.; Hu, X.; Zhou, F.; Qiu, Y.; Li, M.; Huang, G. Influence of Temperature on the Interaction of Metal Veins and Hydraulic Fractures in Shale Formations: Experiment and Simulation. *J. Pet. Sci. Eng.* **2021**, *200*, 108372. [CrossRef]
60. Sharma, P.; Prakash, R.; Abedi, S. Effect of Temperature on Nano- and Microscale Creep Properties of Organic-Rich Shales. *J. Pet. Sci. Eng.* **2019**, *175*, 375–388. [CrossRef]
61. Sun, Y.; Bai, F.; Liu, B.; Liu, Y.; Guo, M.; Guo, W.; Wang, Q.; Lü, X.; Yang, F.; Yang, Y. Characterization of the Oil Shale Products Derived via Topochemical Reaction Method. *Fuel* **2014**, *115*, 338–346. [CrossRef]
62. Zuo, J.; Xie, H.; Dai, F.; Ju, Y. Three-Point Bending Test Investigation of the Fracture Behavior of Siltstone after Thermal Treatment. *Int. J. Rock Mech. Min. Sci.* **2014**, *70*, 133–143. [CrossRef]
63. Meredith, P.G.; Atkinson, B.K. Fracture Toughness and Subcritical Crack Growth during High-Temperature Tensile Deformation of Westerly Granite and Black Gabbro. *Phys. Earth Planet. Inter.* **1985**, *39*, 33–51. [CrossRef]
64. Ranjith, P.G.; Viete, D.R.; Chen, B.J.; Perera, M.S.A. Transformation Plasticity and the Effect of Temperature on the Mechanical Behaviour of Hawkesbury Sandstone at Atmospheric Pressure. *Eng. Geol.* **2012**, *151*, 120–127. [CrossRef]
65. Tang, H.; Kang, Z.; Wang, K. Real-Time Evolution of Oil Shale Meso-Structure under Triaxial Stress Condition. In Proceedings of the E3S Web of Conferences, Hangzhou, China, 19–21 March 2021; EDP Sciences: Les Ulis, France, 2021; Volume 248.